ADVANCED FUNCTIONAL MATERIALS
www.afm-journal.de

Thin-Wall Assembled SnO_2 Fibers Functionalized by Catalytic Pt Nanoparticles and their Superior Exhaled-Breath-Sensing Properties for the Diagnosis of Diabetes

*Jungwoo Shin, Seon-Jin Choi, Inkun Lee, Doo-Young Youn, Chong Ook Park, Jong-Heun Lee, Harry L. Tuller, and Il-Doo Kim**

Hierarchical SnO_2 fibers assembled from wrinkled thin tubes are synthesized by controlling the microphase separation between tin precursors and polymers, by varying flow rates during electrospinning and a subsequent heat treatment. The inner and outer SnO_2 tubes have a number of elongated open pores ranging from 10 nm to 500 nm in length along the fiber direction, enabling fast transport of gas molecules to the entire thin-walled sensing layers. These features admit exhaled gases such as acetone and toluene, which are markers used for the diagnosis of diabetes and lung cancer. The open tubular structures facilitated the uniform coating of catalytic Pt nanoparticles onto the inner SnO_2 layers. Highly porous SnO_2 fibers synthesized at a high flow rate show five-fold higher acetone responses than densely packed SnO_2 fibers synthesized at a low flow rate. Interestingly, thin-wall assembled SnO_2 fibers functionalized by Pt particles exhibit a dramatically shortened gas response time compared to that of un-doped SnO_2 fibers, even at low acetone concentrations. Moreover, Pt-decorated SnO_2 fibers significantly enhance toluene response. These results demonstrate the novel and practical feasibility of thin-wall assembled metal oxide based breath sensors for the accurate diagnosis of diabetes and potential detection of lung cancer.

1. Introduction

Selective detection of specific volatile organic compounds (VOCs) in exhaled breath is a very attractive non-invasive diagnostic tool for the fast and simple recognition of various diseases, including diabetes[1–9] and lung cancer.[10–13] In particular, the breathing diagnosis for diabetes is largely based on an acetone breath test.[4] Acetone concentration in exhaled breath varies due to an anomaly of metabolism related to the incomplete management of glucose in blood, as well as the production of a high level of fatty acids which are transformed into ketone bodies in the liver.[4,14–18] These ketones are very volatile compounds, so they can be easily vaporized in the breathing process. The exhaled acetone level of diabetes patients is found to exceed 1.8 ppm, which is 2 to 6 fold higher than that (0.3–0.9 ppm) of healthy people.[3,19] Thus, a superior detection sensitivity to acetone below 1 ppm, in the presence of other exhaled gases, is necessary for the accurate diagnosis of diabetes, especially under a highly humid environment (relative humidity (RH) > 80%). In addition, a trace concentration of toluene (30 ppb) in exhaled breath is regarded to be a distinctive early symptom of lung cancer.[13]

Until now, various gas sensing techniques have been widely used to analyse a number of VOCs, including gas chromatography (GC),[20] mass chromatography (MC)[21] ion mobility spectrometry (IMS)[22] and selected ion flow tube mass spectrometry (SIFT-MS).[23,24] However, they are hard to incorporate into portable real-time gas sensors because of the large size of the equipment, their complexity of operation and high cost.[25–32] On the other hand, metal oxide based chemiresistive gas sensors can offer greater usability for portable real-time breath sensors thanks to their miniaturized size, low cost, easy fabrication and simplicity of operation.[33–39] Moreover, recent progress in the synthesis of novel nanostructures can be adopted to develop high sensitivity breathing sensors, because their superior surface area, as well as pore size and distribution, have crucial roles in the interaction between sensing layers and target VOC gases. These nanostructures include nanoparticles, hollow spheres, 1D nanostructures such as tubes, wires, and fibers, and their hierarchically assembled structures. Among them, 1D metal oxide nanostructures have been identified as one of the most effective nanoarchitectures for chemiresistive sensors due to their large surface area to volume ratio, high gas accessibility and good thermal stability.[40–51]

J. Shin, S.-J. Choi, I. Lee, D.-Y. Youn, Dr. C. O. Park, Dr. I.-D. Kim
Department of Materials Science and Engineering
Korea Advanced Institute of Science and Technology
291 Daehak-ro, Yuseong-gu, Daejeon 305-701, Republic of Korea
E-mail: idkim@kaist.ac.kr
Dr. J.-H. Lee
Department of Materials Science and Engineering
Korea University
Anam-Dong, Seongbuk-Gu, Seoul 136-713, Republic of Korea
Dr. H. L. Tuller
Department of Materials and Engineering
Massachusetts Institute of Technology
Cambridge, MA 02139, USA

DOI: 10.1002/adfm.201202729

In terms of the facile synthesis of 1D metal oxide nanostructures, electrospinning is one of the most simple and versatile methods for producing polycrystalline metal oxide fibers from a rich variety of materials, due to its easy process control of morphological evolution and compositional manipulation.[52,53] Thus far, several approaches have been suggested for the morphological control of electrospun fibers including hollow tubes, porous fibers and core-shell structures.[53] Among them, the phase separation effect during the formation of an electrospun jet has been studied widely in order to understand the underlying mechanism influencing the creation of unique morphologies. The phase separation process of electrospun fibers results from the hydrolysis, condensation and gelation of precursors under the rapid elongation of polymers while volatile solvents are evaporated, within milliseconds. Spinodal phase separation, with distinct chemical composition, takes place as the result of unstable fluctuations due to precursor gradients inside fibers,[54,55] resulting in unique fiber morphologies, including porous polymethylsilsesquioxane (PMSQ) fibers, wrinkled polystyrene (PS) fibers, 3D porous gelatin (Gt) and polycaprolactone (PCL) fibers.[56–65] In particular, the phase separation process of electrospun fibers consisting of ceramic precursors and polymers often leads to the formation of highly porous ceramic fibers, after the elimination of polymer-rich regions and the crystallization of the ceramic precursors. These inorganic fibers include fibers composed of multiple TiO_2 nanowires,[51] lotus-root shaped Zn_2SnO_4 fibers,[42] hollow ZnO nanofibers,[66] rice grain shaped TiO_2 mesoporous structures,[67] silica nanotubes,[68] etc. In addition, novel nanostructures consisting of various types of pores and discontinuous segments have been achieved through the precise control of various key factors, i.e., a) the miscibility of polymer,[55,56,62–66] b) humidity,[57] c) liquid-liquid miscibility,[58,59,71] d) a phase-separation-inducing agent,[60] e) the solubility difference between precursors and polymers,[42,66–68] f) volatile solvent[61,69,70] and g) flow-rate. The effect of flow rate on the morphologies of electrospun fibers has been predicted by Wendorff et al.[71] who suggested its effect on the alignment of polymer chains of the electrospun fiber. Dayal and Kyu[54] also predicted the influence of flow rate on the phase separation process by chemical concentration sweep with the mathematical model of "wiggling motion". Nevertheless, no practical demonstration involving flow rate induced phase separation has been conducted to the best of our knowledge.

In this paper, we report the morphological evolution of SnO_2 fibers, composed of wrinkled thin SnO_2 nanotubes, produced by the variation of flow rate during electrospinning, and the effect of catalytic Pt nanoparticle decoration on the enhancement of their sensing properties toward acetone and toluene in exhaled breath. The phase separation behaviors between tin precursors and polymers, which are influenced by the control of flow rates (low, intermediate and fast), can significantly change the morphologies of SnO_2 fibers, whose calcination produces the crystallization of ceramic precursors and burn-out of immiscible polymers. In particular, elongated open pores are extensively formed on the surface of the thin-walls of wrinkled SnO_2 tubes. This unique morphological feature can significantly increase the accessibility of the entire sensing layers to exhaled breath gas. Thanks to the high gas permeability of SnO_2 fibers synthesized at 25 μL min^{-1} a superior detecting capacity with appreciable response (R_{air}/R_{gas}–1 = 0.72) was achieved at very low acetone concentration (120 ppb). After combining with Pt catalytic nanoparticles, short response (<11 s) and recovery times (<6 s) were obtained upon exposures to acetone and humid air, demonstrating its potential for a fast-responding breath diagnosis diabetes sensor.

2. Results and Discussion

2.1. Synthesis and Morphological Characterization of Dense and Porous SnO_2 Fibers

The procedures to prepare pure and Pt-loaded SnO_2 fibers are illustrated in **Figure 1**. Tin (IV) acetate (0.5 g), PVAc (0.333 g, 500,000 g mol^{-1}), DMF (2 mL) and acetic acid (0.066 g) were chosen as basic components, because the poor compatibility of tin (IV) acetate and PVAc in DMF solvent can provide porous structures after the oxidation of Sn precursors and burn-out of immiscible polymers.[41–43] The flow rates of each electrospinning process were adjusted to 5 μL min^{-1}, 15 μL min^{-1} and 25 μL min^{-1}, respectively. As-spun fiber mats were collected on stainless steel substrate and calcined to develop the pores and voids inside the SnO_2 fibers, by removing the phase-separated polymer-rich regions.[51,55,56,66–68] As shown in Figure 1a, as-spun tin precursor/PVAc composite fibers prepared at the low flow rate (5 μL min^{-1}) showed a smooth surface morphology with uniformly mixed coiled polymers and tin precursors inside. During calcination, polymers were transformed to carbon dioxides and water vapor, and the tin precursors were crystallized into polycrystalline SnO_2, which consisted of small nanoparticles. As the flow rate was increased, the surface

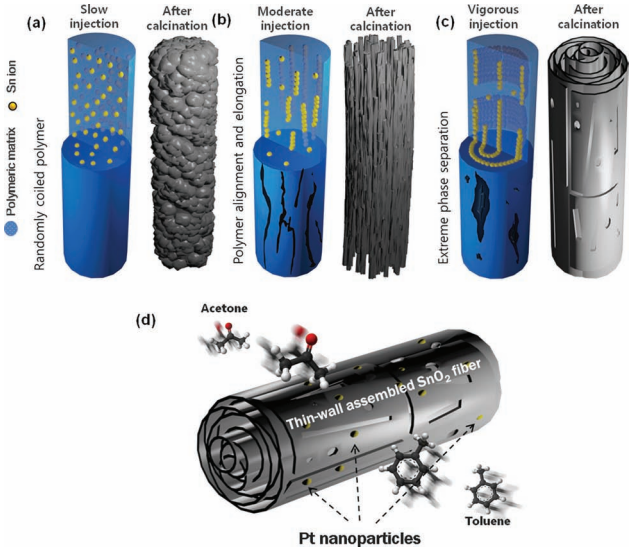

Figure 1. Schematic illustration of morphological evolution of as-spun and calcined SnO_2 fibers prepared at different flow rates: a) 5 μL min^{-1}, b) 15 μL min^{-1}, and c) 25 μL min^{-1}; and d) Pt-decorated thin-wall assembled SnO_2 fibers.

morphologies of the as-spun fibers were significantly changed and polymer chains inside the fibers were elongated along the longitudinal direction of the fibers, due to the increased tensile stress of the jet. In the case of an intermediate flow rate (15 μL min^{-1}), as-spun fibers had a number of wrinkled stripes along the fiber direction (Figure 1b, left). After heat treatment at high temperature, the fibers showed more porous bundle-type structures with elongated SnO_2 fibrils (Figure 1b, right). As-spun fibers synthesized at a high flow rate (25 μL min^{-1}) had a wide range of carved valleys on the fiber surface (Figure 1c, left). After calcination at 500 °C, highly porous SnO_2 fibers were obtained having a number of elongated open pores, and inner walls containing large voids between them (Figure 1c, right). Figure 1d shows the schematic illustration of Pt-loaded SnO_2 fibers composed of wrinkled thin-walled tubes. Because the open tubular structures include elongated pores and large voids between the thin tubes, Pt catalysts with tiny size (4–7 nm) can be uniformly decorated on and even inside the SnO_2 fibers, leading to very effective functionalization of the entire, large surface area.

Figure 2 shows the microstructural evolutions of as-spun tin precursors/PVAc and calcined SnO_2 fibers, as a function of flow rate. Smooth surfaced as-spun fibers with an average diameter of 230 nm were prepared at the injection rate of 5 μL min^{-1} (Figure 2a). At the slow injection rate, tin precursors and PVAc were presumably less affected by kinetic factors driven by the flow injection. After calcination at 500 °C, typical densely packed SnO_2 fibers were obtained (Figure 2b).[41–43] During the calcination process tin precursors were transformed into spherical SnO_2 particles, which are most thermodynamically stable form in the absence of an external driving force, while the PVAc was burned out. As a consequence, polycrystalline SnO_2 fibers composed of very fine SnO_2 nanoparticles were obtained (Figure 2c). The rutile structure of the fine polycrystalline SnO_2 fibers were confirmed by ring electron diffraction patterns (Figure 2c, inset).

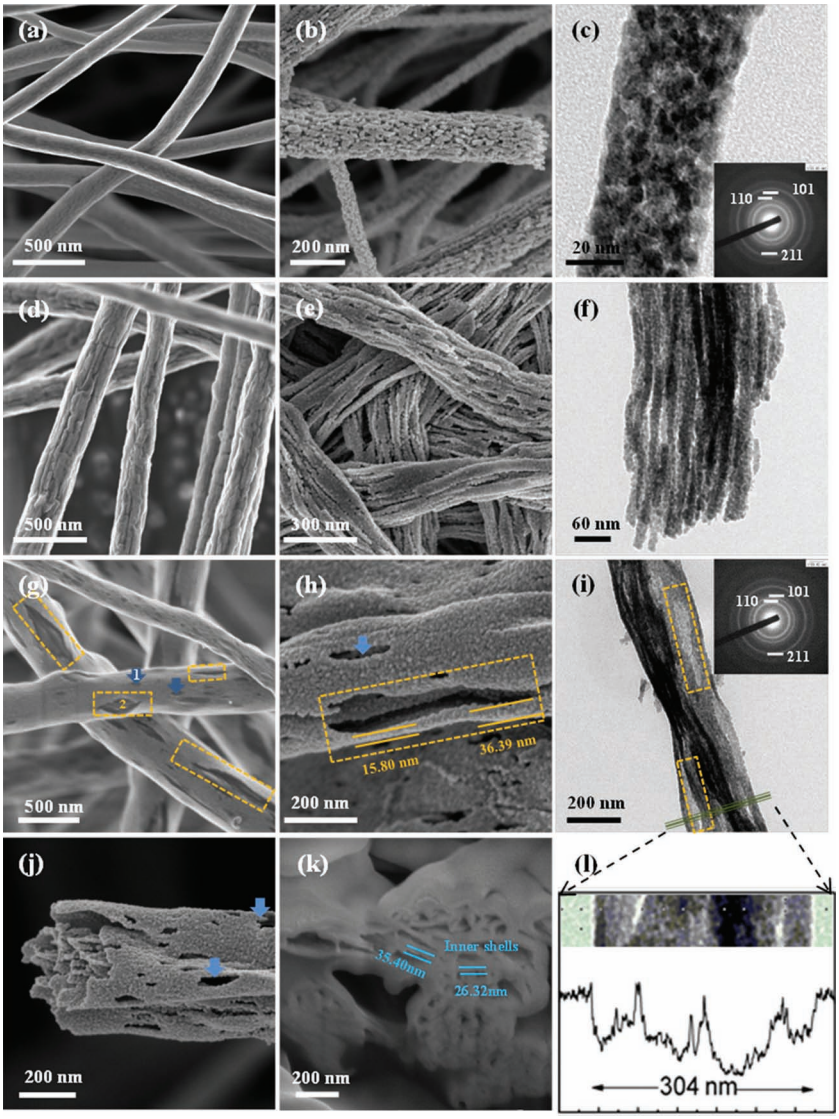

Figure 2. a) SEM image of the as-spun fibers (5 μL min^{-1}). b) SEM image of densely packed SnO_2 fibers after calcination at 500 °C (5 μL min^{-1}). c) TEM image of densely packed SnO_2 fiber. Inset image shows SAD pattern of corresponding fiber. d) SEM image of the as-spun fibers (15 μL min^{-1}). e) SEM image of the multi-fibrous fibers after calcination at 500 °C (15 μL min^{-1}). f) TEM image of a multi-fibrous fiber. g) SEM image of the as-spun fiber (25 μL min^{-1}). The blue arrows, labeled 1, indicate small dimples on fiber. The yellow dotted frames, labeled 2, show crevices stretched along the longitudinal direction. h) SEM image of the thin-wall assembled SnO_2 fibers after calcination at 500 °C (25 μL min^{-1}). The blue arrow and yellow dotted frames indicate the fibers have multiple small pores and elongated open pores. Yellow parallel lines denote each layer's thickness is approximately 30 nm. i) TEM image of a thin-wall assembled SnO_2 fiber. j) Magnified SEM image of a broken thin-wall assembled SnO_2 fiber. k) FIB-cut image of thin-wall assembled SnO_2 fibers. l) Intensity profile across a thin-wall assembled SnO_2 as shown in (i).

Increasing the flow rate to 15 μL min^{-1} induced dramatic changes in the shape of the as-spun fibers (Figure 2d). The as-spun fibers had elongated wrinkles and stripes along the fiber direction. After heat treatment, crumpled furrows were developed into the aligned gaps between multiple polycrystalline SnO_2 rods within the fibers (Figure 2e). The significant morphological difference originated from the change in kinetic behavior of the electrospun jet by "wiggling motion".[54] The increased flow rate along the longitudinal direction could increase the surface tension of the polymeric matrix in the axial direction, leading to wrinkling of the fiber surface. In addition, because of the propensity for tin (IV) acetate precursors in DMF solution to have low compatibility with PVAc polymer, the polymeric matrix and tin precursors can undergo microphase separation, if sufficient fluctuation-driving force, i.e., flow rate, is given. Thus, the multirod-like morphology of the

long, elongated PVAc chains and tin precursors, which filled the aligned gap between elongated polymeric matrixes along the longitudinal direction, can be preserved after calcination (Figure 2f).

The morphology was further evolved at the higher flow rate. When given an extremely fast injection rate, the as-spun jet can be markedly elongated in the longitudinal direction of the fibers.[72,73] The increased amount of solvent injected through the needle leads to a massive evaporation of solvent per time, which enables the components inside the electrospun fiber to undergo unstable fluctuations. Consequently, the degree of phase separation was further intensified when an extremely fast flow rate was applied, leading to greater changes in morphology. In addition, the diameter of the as-spun fibers can be increased as the flow rate increases, due to the large amount of solution that is being injected.

The blue arrows, 1, and dotted yellow frames, 2, in Figure 2g indicate that as-spun fibers synthesized at 25 μL min^{-1} had small dimples and even larger crevices extending along the longitudinal direction on the surface of the fibers. The contrast difference between the surface of the fibers and the inside of the crevices indicates that the inside is composed of polymer-rich phase. The phase separation between this distinguishing polymeric matrix and tin precursors was confirmed by the appearance, in the dotted yellow frames, of elongated open pores after the burning out of all polymers in the crevice at elevated temperatures (Figure 2h). Average thickness of the outer layers at the crevice was approximately 30 nm. The elongated open pores, where the polymer-rich phase was removed, were also seen as bright parts (the dotted yellow frames in Figure 2i, and l, which is the transmittance intensity plot of Figure 2i).

For the remainder of this paper, SnO_2 fibers synthesized at 5 μL min^{-1}, and 25 μL min^{-1}, will now be denoted as densely packed, and thin-wall assembled fibers, respectively. Figure 2j is a magnified SEM image of a broken thin-wall assembled SnO_2 fiber. The close view of a cross section reveals the existence of inner layers as well as large voids on individual walls. This image clearly demonstrates that highly porous fibers, which are assembled with wrinkled SnO_2 tubes, were successfully synthesized. Small pores indicated by the blue arrows in this image are believed to be developed not only from the small dimples in the as-spun fibers, but also created by CO_2 or H_2O gases arising from the degradation and combustion of polymers between the inner walls during heat treatment. The average thickness of the inner layers was similar to that of the outer shell (30 nm), as indicated in the focused ion beam (FIB) image (Figure 2k). The porous inner and outer layers enable gas molecules to pass through the outer layers and to reach inner active surfaces more easily than the densely packed SnO_2 fibers (Figure 2b). The variety in size and shape of the inner walls of the thin-wall assembled SnO_2 fibers can provide particular superiority in gas responses compared to the densely packed SnO_2 fibers. For comparison, FIB images of SnO_2 fibers prepared at flow rates of 5 μL min^{-1} and 15 μL min^{-1} are shown in Supporting Information Figure S2. In the case of SnO_2 fibers (15 μL min^{-1}), bundles of inner rods were observed instead of inner walls. The SnO_2 fibers (5 μL min^{-1}) exhibited densely packed morphologies without any distinguishable large voids.

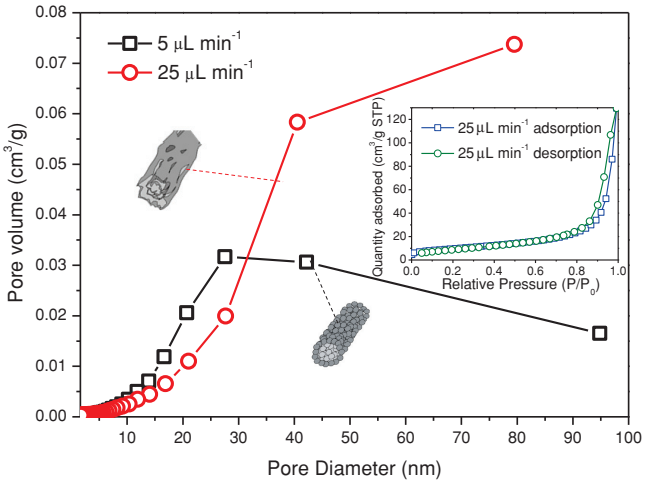

Figure 3. Pore volume distribution of SnO_2 fibers synthesized at flow rates of 5 μL min^{-1} and 25 μL min^{-1} observed by Brunauer-Emmett-Teller (BET) measurement. Inset is isothermal adsorption/desorption plot of thin-wall assembled SnO_2 fibers (25 μL min^{-1}).

2.2. Phase Analysis and Crystallization Behavior of SnO_2 Fibers

To investigate the crystallization behavior of SnO_2 fibers, FT-IR measurement, TG/DSC measurement and XRD measurement were performed (Supporting Information Figure S3). For as-spun fibers, absorbance peaks corresponding to the bonding energy of DMF, PVAc and acetic acid were observed by FT-IR measurement. After calcination at 500 °C, those peaks, as well as carbon residues of the calcined fibers, disappeared. From the DSC curve of the as-spun fibers, three major exothermic peaks indicate burn out of PVAc and crystallization of SnO_2.[41,74] After calcination at 500 °C, no particular weight loss or thermal reaction was observed, confirming the formation of crystalline phase rutile SnO_2 (Supporting Information Figure S4).

The pore size distribution of SnO_2 was determined by nitrogen adsorption and desorption (**Figure 3**). For densely packed SnO_2 fibers (5 μL min^{-1}), mesopores, which originated from voids between the small SnO_2 nanoparticles comprising the densely packed SnO_2 fibers, ranged from 10 nm to 30 nm are mainly distributed in greater quantity. In contrast, the pore distribution of thin-wall assembled SnO_2 fibers (25 μL min^{-1}) are mainly larger scale (>30 nm). This can be explained by the elongated open pores and large voids between the walls inside fibers, which can play a key role in enhancing gas accessibility. Especially, the large voids, which exist between thin-walled SnO_2 layers, facilitate the fast in- and counter-diffusion of analyte and product gases, while open pores on each wall offer additional gas penetrating pathways for activating SnO_2 walls, to the innermost layer.

2.3. Microstructure and Chemical State Analysis of Catalytic Pt-Decorated SnO_2 Fibers

Gas response time, which is a very important parameter in exhaled breath sensors, should be shorter than 15 sec. because of the limited breathing capability of patients. Considering

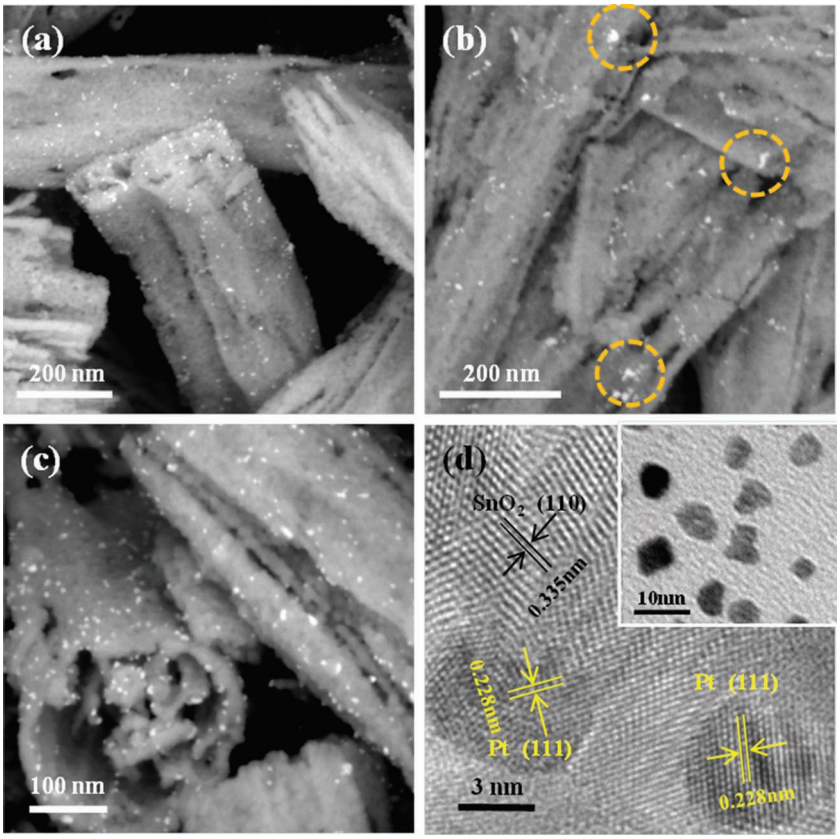

Figure 4. Back scattered electrons (BSE) images of: a) 5 wt%, b) 10 wt%, and c) 20 wt% Pt-decorated thin-wall assembled SnO_2 fibers. Very small portions of aggregated Pt particles less than 20 nm were observed (dotted yellow circles in (b)). d) HRTEM image of Pt-decorated SnO_2 fibers. Inset is TEM image of as-prepared Pt nanoparticles.

that the response and recovery reactions are determined by the in-diffusion of gas and surface reactions, the response and recovery speeds of the sensors with gas-accessible morphology can be significantly improved by the promotion of surface reaction via catalytic decoration.[75] Here, we used Pt nanoparticles synthesized by the polyol method as the catalytic promoters. Thin-wall assembled SnO_2 fibers and Pt catalysts were mixed together using a pestle and mortar. The homogeneous mixing of Pt nanoparticles with SnO_2 fibers was confirmed by back scattered electron (BSE) images. **Figure 4**a-c show the BSE images of 5, 10 and 20 wt% Pt-decorated thin-wall assembled SnO_2 fibers, respectively. Bright dots denote the existence of Pt particles on the surface of SnO_2 fibers. Figure 4c reveals that the inner shells of SnO_2 fiber were uniformly decorated with Pt particles as well. Lattice distances of (110) plane of SnO_2, (0.335 nm)[47] and (111) plane of Pt (0.228 nm)[76] are clearly shown in the HRTEM image (Figure 4d). The inset image emphasizes a TEM image of as-prepared Pt particles.

Pt can be converted into PtO when exposed to oxygen at elevated temperatures. PtO exhibits the p-type semiconductor property with a band gap of 0.86 eV,[76] as opposed to the n-type SnO_2 (3.6 eV). A p-n junction can be formed at the interface between SnO_2 fibers and PtO nanoparticles. The survey-scanned X-ray photoelectron spectroscopy (XPS) spectrum of Pt-decorated SnO_2 fibers is shown in **Figure 5**a with all components including Sn, O and Pt. The PtO spectra was almost absent in as-prepared Pt-decorated SnO_2 fibers (Figure 5b), whereas, in the case of calcined Pt-decorated SnO_2 fibers, the wide spectra of $4f_{7/2}$ energy of PtO as well as a sharp peak of $4f_{7/2}$ energy of Pt were observed at 72.2 eV and 71.2 eV, respectively (Figure 5c).[77,78] A spin-orbit coupling energy between Pt $4f_{5/2}$ and $4f_{7/2}$ is 3.3 eV. The result verifies the partial oxidation of Pt catalysts. Thus, partially oxidized PtO_x can create p–n junctions on the large surface area of SnO_2 fibers. Because thin-wall assembled SnO_2 fibers possess multiple layers with large voids between them, the uniform loading of oxidized Pt nanoparticles will enhance the gas response to a significant degree by extending the electron depleted region of SnO_2 fibers beneath PtO nanoparticles or Pt-PtO core-shell nanoparticles. In addition, Pt and PtO nanoparticles exposed to trace gas can play an important role in the enhancement of gas response by chemical sensitization.

2.4. Gas-Sensing Characteristics

In order to investigate the advantages of thin-wall assembled SnO_2 fibers as an exhaled breath sensor, we carried out acetone and toluene sensing tests. **Figure 6**a shows the sensor resistance in air (R_{air}) of 5 different sensors, i.e., densely packed SnO_2 fibers, thin-wall assembled SnO_2 fibers and 5%, 10% and 20% Pt-decorated SnO_2 fibers, measured at 300 °C and 400 °C. Figure 6b-c exhibit gas sensing responses ($R_{air}/R_{gas} - 1$) of thin-wall assembled and Pt-decorated thin-wall assembled SnO_2 fibers at cyclic exposures to acetone (2 ppm) and toluene (2 ppm) from 200 °C to 400 °C.

Densely packed SnO_2 fibers showed the R_{air} value of 2.2 kΩ while thin-wall assembled SnO_2 fibers had a three-fold higher R_{air} (6.6 kΩ) probably due to the extended electron depleted regions arising from oxygen adsorption on each layer (Figure 6a). The Pt-decorated thin-wall assembled SnO_2 fibers showed a dramatic increase in R_{air} compared to the pure thin-wall assembled SnO_2 fibers. This result might be attributed to the formation of depletion layers from p-n junctions between p-type PtO and n-type SnO_2. The electronic interaction between PtO_x and the SnO_2 surface can be supported again by the observed increase of R_{air} with increasing Pt-loading concentration. As temperatures increased to 400 °C, the R_{air} values of each of the SnO_2 fibers increased. In particular, Pt-decorated SnO_2 fibers showed a dramatic increase in resistivity (>30-fold higher resistance). The remarkable increase in R_{air} of Pt-decorated SnO_2 fibers might be attributed to thermal scattering effects as temperature goes up. The main reason for the higher R_{air} at 400 °C might be explained either by the increased formation of p–n junctions due to the promotion of Pt oxidation, or by the increase of O^- adsorption over O_2^- adsorption, although

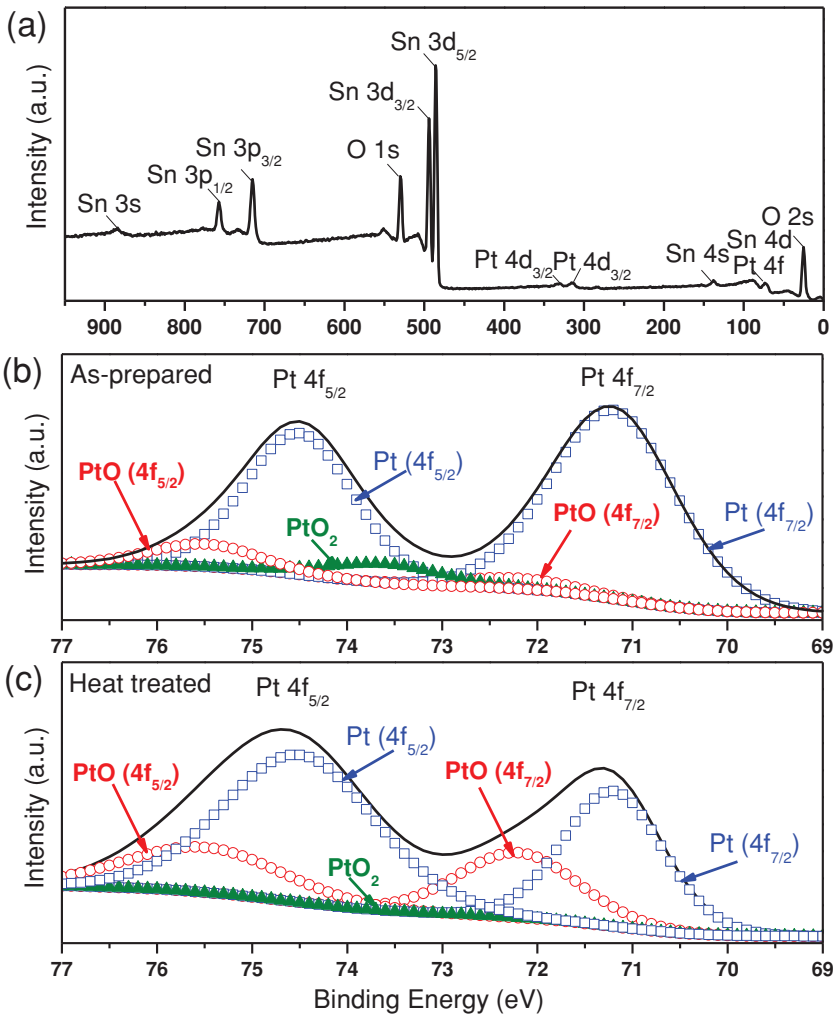

Figure 5. X-ray photoelectron spectroscopy spectra of a) 20 wt% Pt-decorated thin-wall assmebled SnO_2 fibers, b) as-prepared Pt-decorated SnO_2 fibers, and c) calcined Pt-decorated SnO_2 fibers.

further detailed study is necessary to confirm this.[79,80] The latter case refers to the fact that oxygen molecules adsorbed on the Pt catalysts are dissociated and diffused into the surface of SnO_2 fibers in the form of oxygen adatoms with mostly the O^- form, thereby greatly increasing sensor resistance.

As displayed in the response plots in Figure 6, thin-wall assembled SnO_2 fibers showed higher gas responses as temperature goes up (Figure 6b) while Pt-decorated SnO_2 fibers had maximum gas responses at 300 °C, followed by decreases in response at 400 °C (Figure 6c). Referring to previous study,[81] the reason for the lowering of the maximum response temperature can be explained by a sensitization effect, which enables a spill-over process involving a large amount of released chemisorbed oxygen in the form of CO_2 or H_2O when exposed to reducing gases, leaving electrons to the conduction band of tin oxide.[82,83] As a result, the maximum response temperature of Pt-decorated SnO_2 fibers can be effectively reduced to 300 °C, compared to pure SnO_2 fibers, which need higher thermal energy to release adsorbed oxygen. The gradual decreases in response after 300 °C for Pt-decorated SnO_2 fibers might be attributed to the early oxidation of analyte gases which can be exclusively oxidized when assisted by Pt before they reach the sensor surface.

Figure 7a shows acetone concentration changes from 3 ppm to 120 ppb as a function of time. Figure 7b exhibits the acetone response of densely packed SnO_2 fibers and thin-wall assembled SnO_2 fibers at the fixed operation temperature of 400 °C during cyclic exposures of acetone. Thin-wall assembled SnO_2 fibers had a 5-fold higher gas response ($R_{air}/R_{gas} - 1 = 6.12$ at 3 ppm) compared to that (1.22 at 3 ppm) of densely packed SnO_2 fibers. While the acetone response of densely packed SnO_2 fibers at 120 ppb was negligible, thin-wall assembled SnO_2 fibers showed outstanding gas response (0.71) due to their high porosity and tubular morphology. An expected detection response of thin-wall assembled SnO_2 fibers is estimated to be 0.251 at 25 ppb, by plotting a log fitted curve in the inset of Figure 7b. Because H_2O molecules can be involved in gas reactions on the surface of SnO_2,[84] SnO_2 sensors are considered inappropriate to sensors operated in the humid atmosphere, especially at the very low analyte gas concentration (<5 ppm). However, this result demonstrates that pure SnO_2 materials could react with ppb-level acetone even in a highly humid atmosphere without any doping and catalyst decoration if fiber morphologies were optimized. Thin-wall assembled SnO_2 fibers showed a 90% response time of 37.3 s, which is 5-fold faster than that of densely packed SnO_2 fibers, at the exposure of 3 ppm of acetone. However, the acetone response time should be shortened further, down to <15 s, for practical application. To enhance gas response kinetics, we introduced catalytic Pt nanoparticles for functionalization of thin-wall assembled SnO_2 fibers.

Figure 8a shows acetone concentration changes from 3 ppm to 120 ppb as a function of time. Figure 8b,c exhibit cyclic acetone responses of densely packed SnO_2 fibers, thin-wall assembled SnO_2 fibers and Pt-decorated (5%, 10%, and 20%) thin-wall assembled SnO_2 fibers measured at 300 °C, respectively. At 3 ppm acetone exposure, thin-wall assembled SnO_2 fibers ($R_{air}/R_{gas}-1 = 1.25$) showed an 8-fold higher response and 24% shorter response time (112 s) than those (0.145, response speed: 141 s) of densely packed SnO_2 fibers even though the overall performances are reduced compared to those measured at 400 °C.

Among Pt-decorated thin-wall assembled SnO_2 fibers, the 5% Pt-decorated sample showed the best performance ($R_{air}/R_{gas} - 1 = 2.47$, response time: 15 s at 3 ppm acetone) to acetone gas. As explained in the Suporting Information Figure S5, thin-wall assembled SnO_2 fibers showed greatly enhanced response and recovery speeds due to their open structure, which enabled the

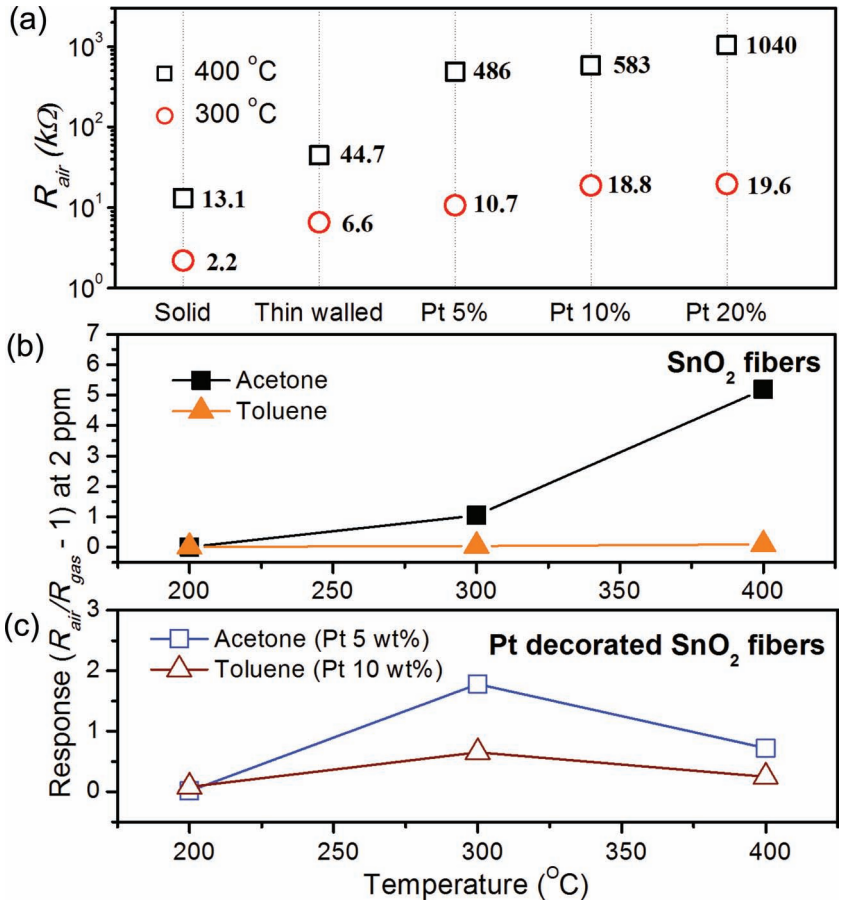

Figure 6. a) Sensor resistances in air (R_{air}) of 5 different sensors at 300 °C and 400 °C. Response dependence of b) thin-wall assembled SnO_2 fibers and c) Pt-decorated SnO_2 fibers on temperatures ranging from 200 °C to 400 °C at cyclic exposure to acetone (2 ppm) and toluene (2 ppm).

fast transport of acetone molecules. In Pt-decorated specimens, the response and recovery times are remarkably shortened. Especially, response times at the concentration range from 200 ppb to 1 ppm are shorter than 11 s, which is beneficial for an exhaled gas sensor for diagnosis of diabetes. The recovery times of the 5% Pt-decorated thin-wall assembled SnO_2 fibers are less than 6 s for a whole range from 120 ppb to 3 ppm. The fast response and recovery speeds are attributed to the activation energy lowering effect assisted by the catalytic coating.[81] The addition of catalytic elements results in the reduced binding energy of Sn3d and O1s and band bending in the near surface of SnO_2, leading to enhanced surface chemical reactions.[85,86]

Figure 8d shows toluene concentration changes from 3 ppm to 120 ppb with respect to time. As shown in Figure 8e pure SnO_2 fibers, either densely packed or thin-wall assembled SnO_2 fibers, showed little response to toluene, whereas Pt-decorated samples exhibited dramatic increases in toluene responses (Figure 8f). Thus, Pt decoration can allow significant selectivity toward toluene because pure SnO_2 fibers do not have any toluene response. This anomaly may be attributed to the promotion of toluene dissociation and its oxidation with negatively charged surface oxygen driven by the Pt catalysts' chemical sensitization effect.

Given the superior performance of the acetone sensing properties and specific selectivity toward toluene gas, we assume it is possible to incorporate the gas sensing layers, including thin-wall assembled SnO_2 fibers functionalized by Pt nanoparticles and pure SnO_2 fibers for a reference, as a non-invasive breath sensor for the diagnosis of lung cancer as well as diabetes.

The gas sensing properties toward acetone and toluene can attract attention because most of other works have only focused on single VOCs sensing properties in a low concentration, due to the limitation in the materials properties. In this report, however, we present a facile, relatively fast turn-over, gas sensing property of SnO_2 fibers, when combined with Pt nanoparticles, down to a very low ppb concentration level. The gas response performance which we have achieved at the lowest concentration is enough to be incorporated in a breath sensor for diabetes detection, which needs an accurate acetone sensing performance between 0.3 ppm to 1.8 ppm. The fast response and recovery time of Pt-decorated thin-wall assembled SnO_2 fibers can enable the potential use of our exhaled breath sensor with a short measurement time. Even though the minimum sensing level of toluene may be not suitable for accurate lung cancer analysis, through further optimizations with materials selection, processing, microstructuring, and functionalizing with various catalysts, we expect to make significant progress in the development of exhaled breath sensors with high accuracy and superior selectivity in the foreseeable future.

3. Conclusions

In summary, thin-wall assembled SnO_2 fibers with wrinkled layers were successfully synthesized by electrospinning with controlled phase separation between precursor-rich phases and polymer-rich phases. The phase separation behaviors between tin precursors and polymers, which are influenced by the control of flow rates (low, intermediate and fast), can significantly change the morphologies of as-spun fibers so that calcination produce the crystallization of ceramic precursors and the burn-out of immiscible polymers. Particularly, elongated open pores are extensively formed on the surface of the wrinkled SnO_2 thin-walls, and hollow voids are found between wrinkled SnO_2 walls. These unique morphological features can make multiple sensing layers within a single fiber accessible, quickly and effectively, to large acetone molecules. In contrast, densely packed SnO_2 fibers that were synthesized at a low flow rate showed poor gas responses. The unique pore distribution and enhanced surface depletion modulation assisted by thin-walled morphologies

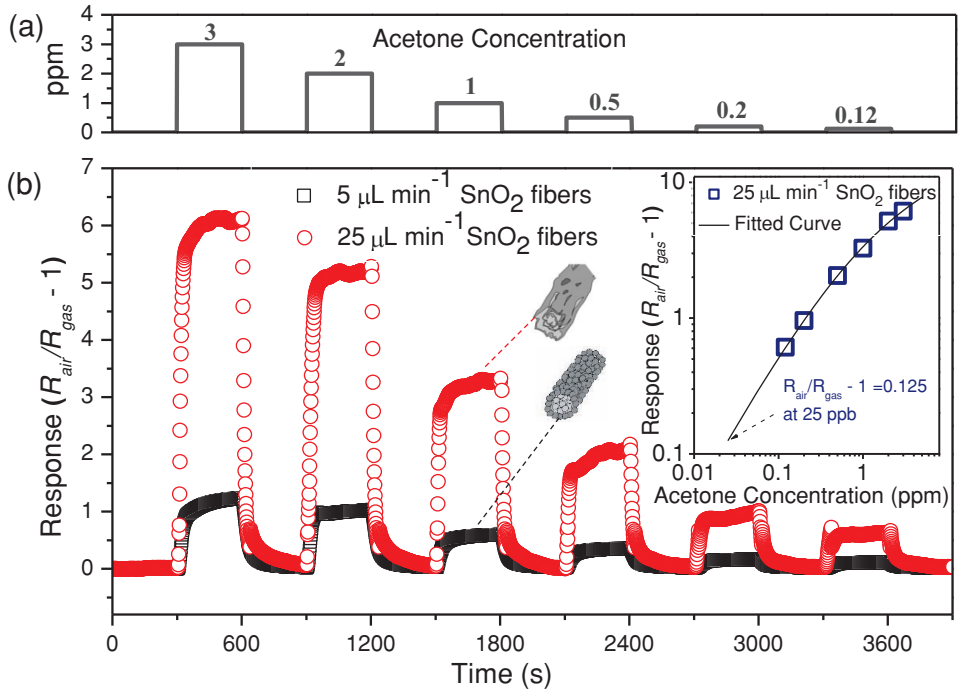

Figure 7. a) The cyclic acetone concentration arranged as 3 ppm, 2 ppm, 1 ppm, 500 ppb, 200 ppb, and 120 ppb with respect to time. b) The acetone response in 80% relative humidity atmosphere at 400 °C of pure SnO_2 fibers synthesized at 5 μL min^{-1} and 25 μL min^{-1}. The inset is the response plot of thin-wall assembled SnO_2 fibers at 400 °C. The black line is log fit curve.

produced the high gas permeability of the SnO_2 fibers synthesized at 25 μL min^{-1}, and a superior detecting capacity with appreciable response ($R_{air}/R_{gas} - 1 = 0.72$) was achieved at low acetone concentration (120 ppb) in highly humid atmosphere (RH 80%). Catalytic Pt-decorated thin-wall assembled SnO_2 fibers demonstrated enhanced acetone response (<11 s) and recovery times (<6 s) at a very low concentration range (0.2–1 ppm) that satisfies the minimum requirement of a real-time diabetes breath diagnosis sensor. Selectivity toward toluene was achieved with Pt decoration as well, while pure SnO_2 fiber sensors showed no toluene response. Here we have verified that thin-wall assembled SnO_2 fibers functionalized by Pt catalysts can be a potential material platform which serves as a gas sensing layer for the diagnosis of diabetes and lung cancer based on exhaled breath, through the detection of acetone and toluene gases.

4. Experimental Section

Synthesis of SnO_2 Fibers: All chemicals used in the electrospinning process were purchased from Aldrich and used as received without any purification. Crystalline SnO_2 fibers with three different morphologies were synthesized as a function of flow rate by electrospinning followed by calcination under air atmosphere. PVAc (0.333 g, 500 000 g mol^{-1}) and tin(IV) acetate (0.5 g) were dissolved in *N,N*-dimethylformamide (2 mL, DMF). Here, DMF was used to increase the tendency toward phase separation where high vapor pressure can significantly induce a rapid driving force after vigorous evaporation of the solvent.[69–71] Low miscibility between tin(IV) acetate and PVAc can effectively induce phase separation, resulting in the precursor-rich and polymer-rich regions, because precursor solutes can be easily segregated into distinct domains by the evaporation of volatile solvent during electrospinning. Since polyvinyl acetate (PVAc) and acetate precursors have been proven to be suitable components for phase separation in previous works,[42,43] we utilized them as a preparation stage to examine flow rate effects. Acetic acid (0.066 g) was added to the solution to improve fiber stability as an adjustment of hydrolysis and gelation of precursors. Then the solution was vigorously stirred with a magnetic bar (500 rpm) at room temperature and subsequently sonicated for 5 min. The mixed solution was loaded into a plastic syringe which was fixed at 15 cm above a grounded collector. A voltage of 16.5 kV was applied from a high-voltage DC power supply to the tip of a stainless steel needle (25 gauge) connected to the syringe. The flow rates were adjusted to 5 μL min^{-1}, 15 μL min^{-1}, and 25 μL min^{-1}, respectively. After electrospinning process, the as-spun fiber mats were collected on stainless steel foil, and immediately brought into an electrical furnace (Vulcan 3–550, Ney) to prevent extended exposure to moisture. The heat treatment temperature was increased from room temperature to 500 °C at 4 °C min^{-1} and kept at 500 °C for 30 min under air atmosphere to ensure the complete removal of carbon residues and to induce crystallization of the SnO_2 fibers.

Synthesis of Catalytic Pt Nanoparticles: Pt catalytic nanoparticles with a size distribution of 4–7 nm were synthesized by the polyol method described by Tekaia-Elhsissen et al.[87] H_2PtCl_6 (0.5 g) was dissolved in an ethylene glycol (5 mL, EG) solution. Then, the H_2PtCl_6/EG solution was slowly injected into a 500 mL flask filled with EG (45 mL) in heated oil bath (150 °C). After 1 hour, 20 mL of polyvinylpyrrolidone (0.5 g, PVP, 10 000 g mol^{-1}) dissolved EG solution was added to the flask at the rate of 2 mL min^{-1}. After another 1 hour, acetone was added into the solution according to a 5: 1 volume ratio of acetone to Pt solution. To isolate Pt particles from the solvent, the mixed solution was centrifuged at 3000 rpm for 5 min and washed with deionized (DI) water multiple times. The black powders obtained were dispersed in ethanol, resulting in the formation of a Pt colloidal solution, which was directly used as a Pt additive source.

Microstructural Characterization: The microstructural evolution of the as-spun fibers and calcined SnO_2 fibers were observed by scanning electron microscope (Field Emission SEM, Magellan400, FEI) and

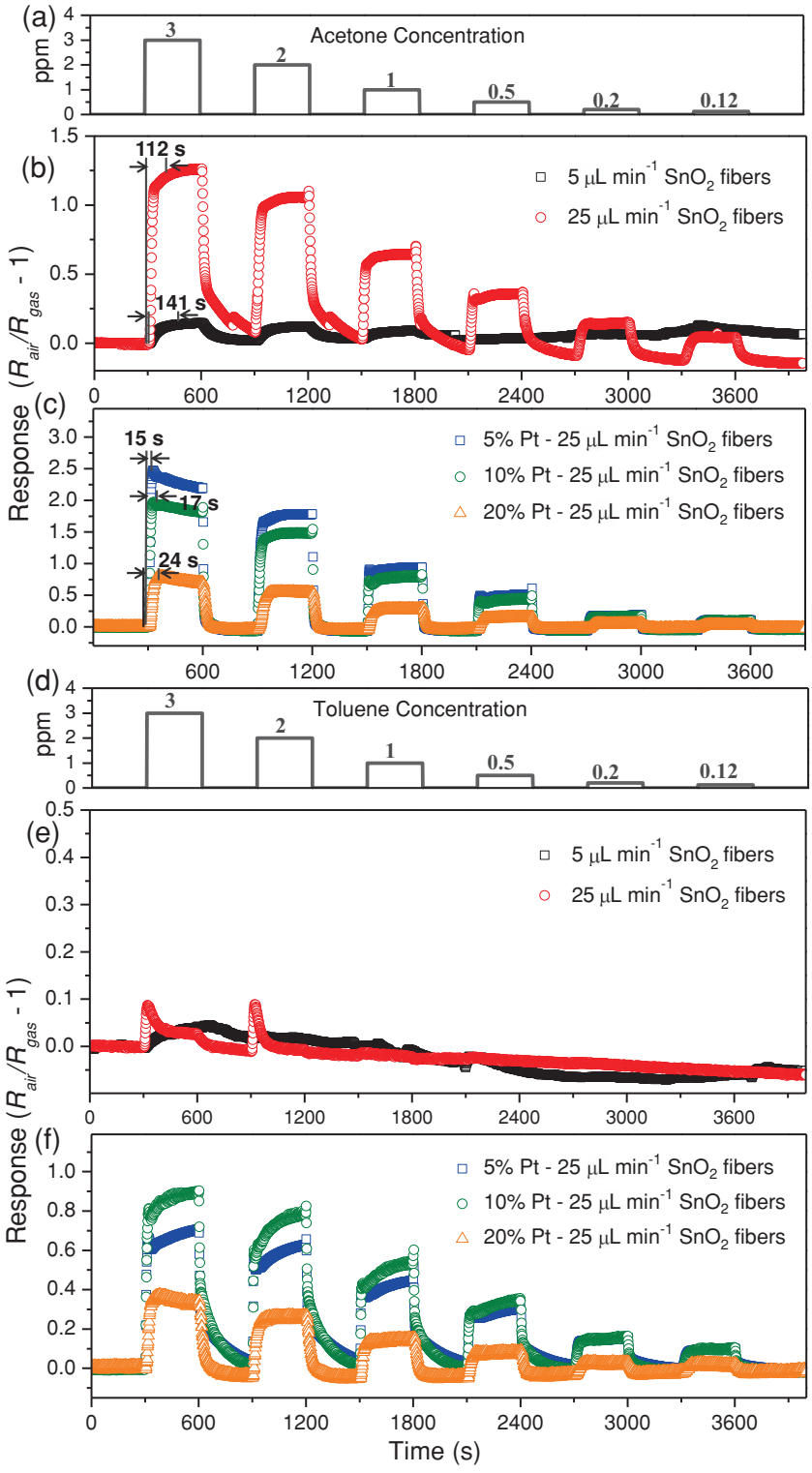

Figure 8. a) The cyclic acetone concentration arranged as 3 ppm, 2 ppm, 1 ppm, 500 ppb, 200 ppb, and 120 ppb with respect to time. The acetone response of b) pure SnO_2 fibers synthesized at 5 μL min^{-1} and 25 μL min^{-1} and c) thin-wall assembled SnO_2 fibers modified with 5 wt%, 10 wt%, and 20 wt% Pt decoration in 80% of relative humidity atmosphere at 300 °C. d) The cyclic toluene concentration arranged as 3 ppm, 2 ppm, 1 ppm, 500 ppb, 200 ppb, and 120 ppb with respect to time. The toluene response of e) pure SnO_2 fibers synthesized at 5 μL min^{-1} and 25 μL min^{-1} and f) thin-wall assembled SnO_2 fibers modified with 5 wt%, 10 wt%, and 20 wt% Pt decoration in 80% of relative humidity atmosphere at 300 °C.

transmission electron microscope (FE-TEM 300KV, Tecnai). The cross section of SnO_2 fibers was investigated by using focused ion beam (FIB, Quanta 3D FEG). The crystal structure of calcined SnO_2 fibers was investigated by X-ray diffraction (D/MAX-2500 series, RIGAKU) patterns using Cu Kα (λ = 1.54 Å) radiation and selected area diffraction (SAD) patterns characterized from TEM analysis. To compare the surface area and porosity of SnO_2 fibers with distinct morphologies synthesized at different flow rates (5 μL min^{-1} and 25 μL min^{-1}), BET measurements (ASAP2020, Micrometrics) were carried out. To check thermal behavior of tin acetate/PVAc composite fibers, thermogravimetric analysis (TGA) and differential scanning calorimetry (DSC) measurements were conducted using Setsys 16/18, Setaram. The complete removal of residual polymers of SnO_2 fibers after heat treatment was confirmed by Fourier transform infrared spectroscopy (FT-IR, IFS66v/s & Hyperion 3000, Bruker). The decorated Pt nanoparticles and their oxidized state were investigated by X-ray photoelectron spectroscopy (XPS, Sigma Probe, Thermo VG Scientific)

Fabrication of Exhaled Breath Sensors: SnO_2 fibers were mixed with PVAc binder with weight ratio of 9: 1, and dropped onto the Au patterned Al_2O_3 substrate (Supporting Information Figure S1) with a heater on the back panel. To provide Pt-decorated SnO_2 fibers, a Pt-ethanol solution was mixed with SnO_2 fibers after calcination and used as a sensing layer. The as-prepared sensors were pressed on a hot plate (80 °C), and dried in a vacuum oven at 80 °C overnight. The sensors were heat-treated at 500 °C for 2 h and stabilized in humid air atmosphere for a week.

Gas Sensing Characterization: Gas sensing experiments were conducted by a home-made device. Gas responses were measured by resistivity changes of sensing layers containing SnO_2 fibers. The humidity was maintained at RH 80%. The heater on the back panel was adjusted at 200 °C 300 °C and 400 °C. The concentrations of acetone and toluene were controlled at 3 ppm, 2 ppm, 1 ppm, 500 ppb, 200 ppb, and 120 ppb in a cycle with a 5 min on/off interval.

Supporting Information

Supporting Information is available from the Wiley Online Library or from the author.

Acknowledgements

This work was supported by a grant from the Ministry of Research, Korea and the Ministry of Science & Technology, Israel. This work was also supported by the Engineering Research Center Program from Korean National Research Foundation. This work was also supported by the Center for Integrated Smart Sensors funded by the Ministry of Education, Science and Technology as Global Frontier Project (CISS-2012M3A6A6054188).

Received: September 19, 2012
Published online: December 13, 2012

[1] J. K. Schubert, W. Miekisch, K. Geiger, *Expert Rev. Mol. Diagn.* **2004**, *4*, 619.
[2] J. B. Yu, H. G. Byun, M. S. So, J. S. Huh, *Sens. Actuators, B* **2005**, *108*, 305.
[3] S. V. Ryabtsev, A. V. Shaposhnick, A. N. Lukin, E. P. Domashevskaya, *Sens. Actuators, B* **1999**, *59*, 26.
[4] D. Smith, P. Spanel, A. A. Fryer, F. Hanna, Gordon A. A. Ferns, *J. Breath Res.* **2011**, *5*, 8.
[5] M. Righettoni, A. Tricoli, S. E. Pratsinis, *Anal. Chem.* **2010**, *82*, 3581.
[6] M. Righettoni, A. Tricoli, *J. Breath Res.* **2011**, *5*, 8.
[7] J. Shi, G. Hu, Y. Sun, M. Geng, J. Wu, Y. Liu, M. Ge, J. Tao, M. Cao, N. Dai, *Sens. Actuators, B* **2011**, *158*, 820.
[8] M. Righettoni, A. Tricoli, S. E. Pratsinis, *Sens. Actuators, B* **2010**, *22*, 3152.
[9] X. Chu, X. Zhu, Y. Dong, X. Ge, S. Zhang, W. Sun, *J. Mater. Sci. Technol.* **2012**, *28*, 200.
[10] G. Peng, U. Tisch, O. Adams, M. Hakim, N. Shehada, Y. Y. Broza, S. Billan, R. Abdah-Bortnyak, A. Kuten, H. Haick, *Nat. Nanotechnol.* **2009**, *4*, 669.
[11] H. J. O'Neill, S. M. Gordon, M. H. O'Neill, R. D. Gibbons, J. P. Szidon, *Clin. Chem.* **1988**, *34*, 1613.
[12] M. Phillips, K. Gleeson, J. M. Hughes, J. Greenberg, R. N. Cataneo, L. Baker, W. P. McVay, *Lancet* **1999**, *353*, 1930.
[13] D. Poli, P. Carbognani, M. Corradi, M. Goldoni, O. Acampa, B. Balbi, L. Bianchi, M. Rusca, A. Mutti, *Respir. Res.* **2005**, *6*, 71.
[14] W. Ping, T. Yi, X. Haibao, S. Farong, *Biosens. Bioelectron.* **1997**, *12*, 1031.
[15] N. Makisimovich, V. Vorotyntyntsev, N. Nikitina, O. Kaskevich, P. Karabun, F. Martynenko, *Sens. Actuators, B* **1996**, *35*, 419.
[16] B. Solnica, J. W. Naskalski, J. Sieradzki, *Clin. Chim. Acta.* **2003**, *331*, 29.
[17] M. Gerard, A. Chaubey, B. D. Malhotra, *Biosens. Bioelectron.* **2002**, *17*, 345.
[18] M. Fleischer, E. Simon, E. Rumpel, H. Ulmer, M. Harbeck, M. Wandel, C. Fietzek, U. Weimer, H. Meixner, *Sens. Actuators, B* **2002**, *83*, 245.
[19] C. H. Deng, J. Zhang, X. F. Yu, W. Zhang, X. M. Zhang, *J. Chromatogr.* **2004**, *810*, 269.
[20] J. M. Sanchez, R. D. Sacks, *Anal. Chem.* **2003**, *75*, 2231.
[21] R. Mukhopadhyay, *Anal. Chem.* **2004**, *76*, 273A.
[22] H. Lord, Y. F. Yu, A. Segal, J. Pawliszyn, *Anal. Chem.* **2002**, *74*, 5650.
[23] D. Smith, P. Spanel, *Mass Spectrom. Rev.* **2005**, *24*, 661.
[24] P. Spanel, D. Smith, *Med. Biol. Eng. Comput.* **1996**, *34*, 409.
[25] M. Hanada, H. Koda, K. Onaga, K. Tanaka, T. Okabayashi, T. Itoh, H. Miyazaki, *Anal. Chim. Acta* **2003**, *475*, 27.
[26] T. Becker, S. Muhiberger, C. B. Braunmuhl, G. Muller, T. Ziemann, K. V. Hechtenberg, *Sens. Actuators, B* **2000**, *69*, 108.
[27] M. Kaneyasu, A. Ikegami, H. Arima, S. Iwanaga, *IEEE Trans. Components, Hybrids, Manuf. Technol.* **1987**, *10*, 267.
[28] A. W. E. Hodgson, P. Jacquinot, P. C. Hauser, *Anal. Chem.* **1999**, *71*, 2831.
[29] K. H. Kim, S. A. Jahan, E. Kabir, *Trends Anal. Chem.* **2012**, *33*, 1.
[30] K. Toda, J. Li, P. K. Dasgupta, *Anal. Chem.* **2006**, *78*, 7284.
[31] A. M. Diskin, P. Spanel, D. Smith, *Physiol. Meas.* **2003**, *24*, 107.
[32] C. H. Deng, J. Zhang, X. F. Yu, W. Zhang, X. M. Zhang, *J. Chromatogr. B* **2004**, *810*, 269.
[33] M. Fleischer, E. Simon, E. Rumpel, H. Ulmer, M. Harbeck, M. Wandel, C. Fietzek, U. Weimar, H. Meixner, *Sens. Actuators, B* **2002**, *83*, 245.
[34] C. D. Natale, A. Macagnano, E. Martinelli, R. Paolesse, G. D'Arcangelo, C. Roscioni, A. Finazzi-Agro, A. D'Amico, *Sens. Actuators, B* **2003**, *18*, 1209.
[35] S. V. Ryabtsev, A. V. Shaposhnick, A. N. Lukin, E. P. Domashevskaya, *Sens. Actuators, B* **1999**, *59*, 26.
[36] L. Wang, A. Teleki, S. E. Pratsinis, P. I. Gouma, *Chem. Mater.* **2008**, *20*, 4794.
[37] G. Eranna, B. C. Joshi, D. P. Runthala, R. P. Gupta, *Crit. Rev. Solid State Mater. Sci.* **2004**, *29*, 111.
[38] M. Graf, D. Barrettino, S. Taschini, C. Hagleitner, A. Hierlemann, H. Baltes, *Anal. Chem.* **2004**, *76*, 4437.
[39] G. Korotcenkov, *Sens. Actuators, B* **2005**, *107*, 209.
[40] L. Mai, L. Xu, Q. Gao, C. Han, B. Hu, Y. Pi, *Nano Lett.* **2010**, *10*, 2604.
[41] I. D. Kim, E. K. Jeon, S. H. Choi, D. K. Choi, H. L. Tuller, *J. Electroceram.* **2010**, *25*, 159.
[42] S. H. Choi, I. S. Hwang, J. H. Lee, S. G. Oha, I. D. Kim, *Chem. Commun.* **2011**, *47*, 9315.
[43] I. D. Kim, A. Rothschild, *Polym. Adv. Technol.* **2011**, *22*, 318.
[44] D. J. Yang, I. Kamienchick, D. Y. Youn, A. Rothschild, I. D. Kim, *Adv. Funct. Mater.* **2010**, *20*, 4258.
[45] X. Wang, Z. Xie, H. Huang, Z. Liu, D. Chen, G. Shen, *J. Mater. Chem.* **2012**, *22*, 6845.
[46] Y. Li, J. Xu, J. Chao, D. Chen, S. Ouyang, J. Yeb, G. Shen, *J. Mater. Chem.* **2011**, *21*, 12852.
[47] Z. Zhang, R. Zou, G. Song, L. Yu, Z. Chen, J. Hu, *J. Mater. Chem.* **2011**, *21*, 17360.
[48] J. Liu, Z. Guo, K. Zhu, W. Wang, C. Zhang, X. Chen, *J. Mater. Chem.* **2011**, *21*, 11412.
[49] J. T. Korhonen, P. Hiekkataipale, J. Malm, M. Karppinen, O. Ikkala, R. H. A. Ras, *ACS Nano* **2011**, *5*, 1967.
[50] J. S. Lee, O. S. Kwon, S. J. Park, E. Y. Park, S. A. You, H. Yoon, J. Jang, *ACS Nano* **2011**, *5*, 7992.
[51] I. D. Kim, A. Rothschild, B. H. Lee, D. Y. Kim, S. M. Jo, H. L. Tuller, *Nano Lett.* **2006**, *6*, 9.
[52] D. Li, J. T. McCann, Y. Xia, *J. Am. Ceram. Soc.* **2006**, *89*, 1861.
[53] Y. Dai, W. Liu, E. Formo, Y. Sun, Y. Xia, *Polym. Adv. Technol.* **2011**, *22*, 326.
[54] P. Dayal, T. Kyu, *Phys. Fluids.* **2007**, *19*, 107106.
[55] M. Bognitizki, T. Frese, M. Steinhart, A. Greiner, J. H. Wendorff, *Polym. Eng. Sci.* **2001**, *41*, 942.
[56] S. O. Han, W. K. Son, D. Cho, J. H. Youk, W. H. Park, *Polym. Degrad. Stab.* **2004**, *86*, 257.
[57] C. L. Pai, M. C. Boyce, G. C. Rutledge, *Macromolecules* **2009**, *42*, 2102.
[58] S. O. Han, W. K. Son, J. H. Youk, T. S. Lee, W. H. Park, *Mater. Lett.* **2005**, *59*, 2998.
[59] Y. Miyauchi, B. Ding, S. Shiratori, *Nanotechnology* **2006**, *17*, 5151.
[60] Y. Hong, X. Chen, X. Jing, H. Fan, Z. Gu, X. Zhang, *Adv. Funct. Mater.* **2010**, *20*, 1503.
[61] M. Bognitzki, W. Czado, T. Frese, A. Schaper, M. Hellwig, M. Steinhart, A. Greiner, J. H. Wendorff, *Adv. Mater.* **2001**, *13*, 70.
[62] C. J. Luo, M. Nangrejo, M. Edirisinghe, *Polymer* **2010**, *51*, 1654.
[63] M. Peng, D. Li, L. Shen, Y. Chen, Q. Zhen, H. Wang, *Langmuir* **2006**, *22*, 9368.
[64] Y. Z. Zhang, Y. Feng, Z. M. Huang, S. Ramakrishna, C. T. Lim, *Nanotechnology* **2006**, *17*, 901.
[65] M. Wei, B. Kang, C. Sung, J. Mead, *Macromol. Mater. Eng.* **2006**, *291*, 1307.
[66] Z. Zhang, X. Li, C. Wang, L. Wei, Y. Liu, C. Shao, *J. Phys. Chem.* **2009**, *113*, 19397.
[67] Y. Shengyuan, Z. Peining, A. S. Nair, S. Ramakrishna, *J. Mater. Chem.* **2011**, *21*, 6541.
[68] W. Wang, J. Zhou, S. Zhang, J. Song, H. Duan, M. Zhou, C. Gong, Z. Bao, B. Lu, X. Li, W. Lan, E. Xie, *J. Mater. Chem.* **2010**, *20*, 9068.
[69] S. Megelski, J. S. Stephens, D. B. Chase, J. F. Rabolt, *Macromolecules* **2002**, *35*, 8456.
[70] C. L. Casper, J. S. Stephens, N. G. Tassi, D. B. Chase, J. F. Rabolt, *Macromolecules* **2004**, *37*, 573.

[71] K. Nayani, H. Katepalli, C. S. Sharma, A. Sharma, S. Patil, R. Venkataraghavan, *Ind. Eng. Chem. Res.* **2012**, *51*, 1761.
[72] P. K. Baumgarten, *J. Colloid Interface Sci.* **1971**, *36*, 71.
[73] J. Doshi, *Ph.D. Thesis*, University of Akron, USA **1994**.
[74] J. Uddin, J. E. Peralta, G. E. Scuseria, *Phys. Rev. B* **2005**, *71*, 155112.
[75] J. Shin, S. J. Choi, D. Y. Youn, I. D. Kim, *J. Electroceram.* **2012**, *29*, 106.
[76] K. W. Park, Y. E. Sung, *J. Appl. Phys.* **2003**, *94*, 7276.
[77] K. Kuribayashi, S. Kitamura, *Thin Solid Films* **2001**, *400*, 160.
[78] K. C. Cho, K. C. Hwang, T. Sano, K. Takeuchi, S. Matsuzawa, *J. Photochem. Photobiol., A* **2004**, *161*, 155.
[79] N. Barsan, U. Weimar, *J. Electroceram.* **2001**, *7*, 143.
[80] L. Castaneda, A. Maldonado, M. L. Olvera, *Sens. Actuators, B* **2008**, *133*, 687.
[81] A. Helwig, G. Muller, G. Sberveglieri, G. Faglia, *Sens. Actuators, B* **2008**, *130*, 193.
[82] R. S. Khadayate, J. V. Sali, P. P. Patil, *Talanta* **2007**, *72*, 1077.
[83] S. Liu, F. Zhang, H. Li, T. Chen, Y. Wang, *Sens. Actuators, B* **2012**, *162*, 259.
[84] N. Barsan, U. Weimar, *J. Phys.: Condens. Matter* **2003**, *15*, R813.
[85] S. Mathusnima, Y. Teraoka, N. Miura, N. Yamazoe, *Jpn. J. Appl. Phys.* **1988**, *27*, 1798.
[86] N. Yamazoe, *Sens. Actuators, B* **1991**, *5*, 7.
[87] F. Bonet, V. Delmas, S. Grugeon, R. Herrera Urbina, P.-Y. Silvert, K. Tekaia-Elhsissen, *Nanostruct. Mater.* **1999**, *11*, 1277.